ARTICLE NO. 79-1460R

C80-117

Higher-Order, Finite-Difference Scheme for Three-Dimensional Transonic Flowfields about Axisymmetric Bodies

20005
20010
20018

Lee-tzong Chen* and D. A. Caughey†
McDonnell Douglas Corporation, St. Louis, Mo.

A higher-order, finite-difference scheme using a third-order shape function is applied to the three-dimensional transonic potential flow problem. Only the first- and cross-derivative terms are more accurately represented than in the conventional second-order accurate schemes. The difference equations are solved by relaxation. Both the convergence rate of the relaxation process and the accuracy for a given number of grid points are improved. The potential equation is solved under an arbitrary, locally defined coordinate transformation, capable of treating general three-dimensional geometries. Numerical results for flowfields about axisymmetric nacelles at angle of attack are presented.

Introduction

SINCE the initial success of Murman and Cole[1] in introducing the type-dependent differencing scheme, this relaxation procedure has been extensively applied to obtain finite-difference solutions for transonic flowfields. However, most of the solutions obtained so far are limited to second-order accurate solutions. For complex geometries, the meshes generated in the body-oriented coordinates may have high degrees of distortion, the local potential gradients may be large, and the accuracies of second-order solutions obtained with a given mesh may suffer. To overcome this difficulty, a higher-order, finite-differencing scheme developed using a third-order shape function is introduced. Within the scheme, the first- and cross-derivatives are more accurately represented than in the conventional, centered, second-order-accurate differencing scheme. Therefore, the transformation matrices and the velocity field are more accurately computed for a given mesh, and the overall accuracy of the solution is thus improved.

In treating complex geometries, Jameson and Caughey[2] and Caughey and Jameson[3] introduced overlapping first-order elements in body-oriented coordinates and developed a finite-volume algorithm to solve transonic potential flowfields around wing-body configurations. The finite-volume algorithm applied local coordinate transformation schemes that uncoupled the grid-generation procedure from the procedure used to solve the governing equation. This feature enhances the capability of the relaxation calculations in handling complex geometries. An alternative and more direct approach was suggested by Chen and Caughey[4] who used a second-order element to solve transonic flowfields about axisymmetric nacelles with centerbodies. In the second-order element formulation, the coefficients of the relaxation equation are in the exact form, but when overlapping first-order elements are used, only the principal parts of those coefficients can be calculated. Therefore, the approach suggested in Ref. 4 has a better capability for handling complex geometries.

In the present paper, the two-dimensional problem considered in Ref. 4 is extended to include three-dimensional effects. Numerical results for flowfields about an axisymmetric nacelle engine inlet at angle of attack will be presented. Reyhner[5] has solved the same problem using an alternative method, namely, solving the full potential equation in the

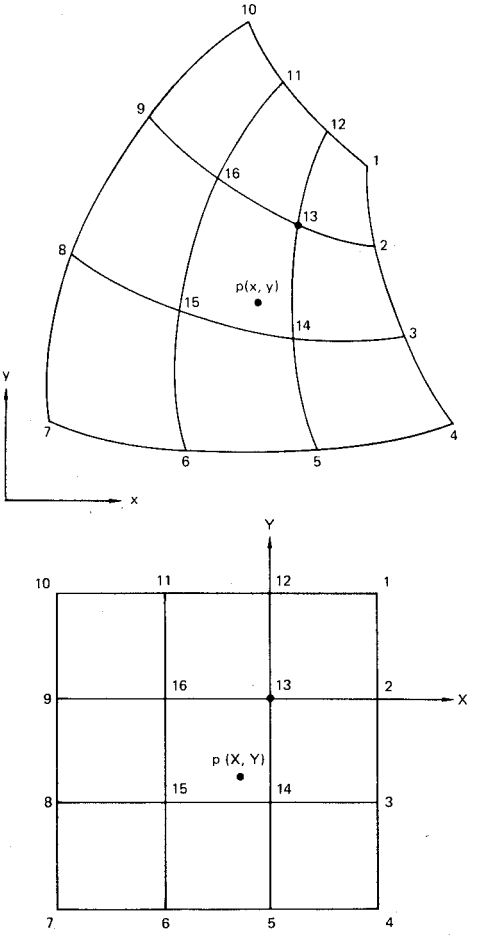

Fig. 1 Transformation of a third-order element; a) physical plane, b) computational plane.

Presented as Paper 79-1460 at the AIAA 4th Computational Fluid Dynamics Conference, Williamsburg, Va., July 23-24, 1979; submitted Aug. 30, 1979; revision received Jan. 8, 1980.

Index categories: Transonic Flow; Channel Flow; Computational Method.

*Research Scientist, McDonnell Douglas Research Laboratories. Member AIAA.

†Consultant, McDonnell Douglas Research Laboratories; Assistant Professor, Sibley School of Mechanical and Aerospace Engineering, Cornell University, Ithaca, N.Y. Member AIAA.

stretched Cartesian coordinates; in his approach, an interpolation scheme is used to treat the body boundary condition and various types of irregular boundary elements, that complicate the treatment of surface boundary conditions, must be considered. In addition, clustering coordinate lines near the body surface in a Cartesian mesh is generally more difficult than in a body-oriented mesh.

Local Coordinate Transformation

To obtain finite-difference solutions in body-oriented coordinates, the (usually) nonuniform physical grid must be transformed to a uniform computational grid. A convenient way is to establish a local coordinate transformation through the application of shape functions. Consider a two-dimensional mesh on the cross section of a three-dimensional grid. Using third-order shape functions, the coordinates x and y of an arbitrary point p in the physical plane (Fig. 1a) are related to the coordinates X and Y in the computational plane by

$$x=\psi^T x_i \tag{1}$$

$$y=\psi^T y_i \tag{2}$$

The column vector of the element shape functions ψ is given as

$$\psi=\frac{1}{36}\begin{Bmatrix} X(X+1)(X+2) & Y & (Y+1)(Y+2) \\ -3X(X+1)(X+2) & (Y-1) & (Y+1)(Y+2) \\ 3X(X+1)(X+2) & Y & (Y-1)(Y+2) \\ -X(X+1)(X+2) & Y & (Y+1)(Y-1) \\ 3(X-1)(X+1)(X+2) & Y & (Y+1)(Y-1) \\ -3X(X-1)(X+2) & Y & (Y+1)(Y-1) \\ X(X+1)(X-1) & Y & (Y+1)(Y-1) \\ -3X(X+1)(X-1) & Y & (Y-1)(Y+2) \\ 3X(X+1)(X-1) & (Y-1) & (Y+1)(Y+2) \\ -X(X+1)(X-1) & Y & (Y+1)(Y+2) \\ 3X(X-1)(X+2) & Y & (Y+1)(Y+2) \\ -3(X-1)(X+1)(X+2) & Y & (Y+1)(Y+2) \\ 9(X-1)(X+1)(X+2) & (Y-1) & (Y+1)(Y+2) \\ -9(X-1)(X+1)(X+2) & Y & (Y-1)(Y+2) \\ 9X(X-1)(X+2) & Y & (Y-1)(Y+2) \\ -9X(X-1)(X+2) & (Y-1) & (Y+1)(Y+2) \end{Bmatrix} \tag{3}$$

$$-1\le X\le 1; \qquad -1\le Y\le 1$$

where ψ^T is the transpose of ψ. The transposes of the column vectors of x and y mesh coordinates are given as

$$x_i^T=[x_1,x_2,\ldots x_{16}] \tag{4}$$

$$y_i^T=[y_1,y_2,\ldots y_{16}] \tag{5}$$

where $(x_1,y_1),(x_2,y_2)\ldots$and (x_{16},y_{16}) are coordinates of points 1,2,...,16 in the physical plane, respectively (see Fig. 1a).

Equations (1) and (2) can be extended to three dimensions in a straightforward manner. These relations can then be applied to perform a coordinate transformation which locally transforms a nonuniform physical grid to a uniform computational grid.

Applying the chain rule, the derivatives of the potential function ϕ in the physical plane are related to their corresponding derivatives in the computational plane by

$$\begin{Bmatrix}\phi_x\\ \phi_y\\ \phi_z\end{Bmatrix}=A\begin{Bmatrix}\phi_X\\ \phi_Y\\ \phi_Z\end{Bmatrix} \tag{6}$$

$$\begin{Bmatrix}\phi_{xx}\\ \phi_{yy}\\ \phi_{xy}\\ \phi_{zz}\\ \phi_{xz}\\ \phi_{yz}\end{Bmatrix}=-BCA\begin{Bmatrix}\phi_X\\ \phi_Y\\ \phi_Z\end{Bmatrix}+B\begin{Bmatrix}\phi_{XX}\\ \phi_{YY}\\ \phi_{XY}\\ \phi_{ZZ}\\ \phi_{XZ}\\ \phi_{YZ}\end{Bmatrix} \tag{7}$$

where

$$A=\begin{bmatrix}x_X & y_X & z_X\\ x_Y & y_Y & z_Y\\ x_Z & y_Z & z_Z\end{bmatrix}^{-1} \tag{8}$$

$$C=\begin{bmatrix}x_{XX} & x_{YY} & x_{XY} & x_{ZZ} & x_{XZ} & x_{YZ}\\ y_{XX} & y_{YY} & y_{XY} & y_{ZZ} & y_{XZ} & y_{YZ}\\ z_{XX} & z_{YY} & z_{XY} & z_{ZZ} & z_{XZ} & z_{YZ}\end{bmatrix}^T \tag{9}$$

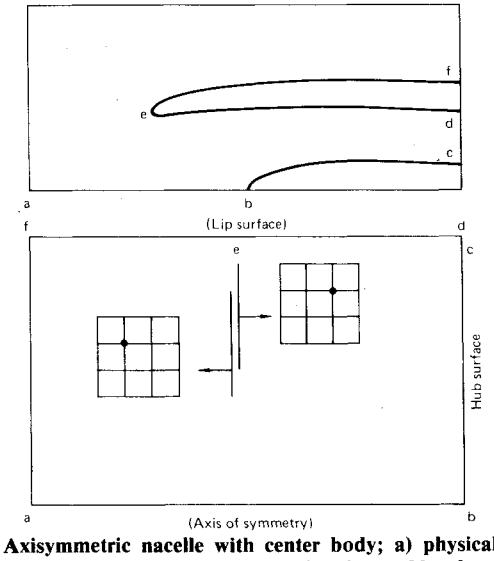

Fig. 2 Axisymmetric nacelle with center body; a) physical plane, b) computational plane, showing sweep direction and local mesh cell.

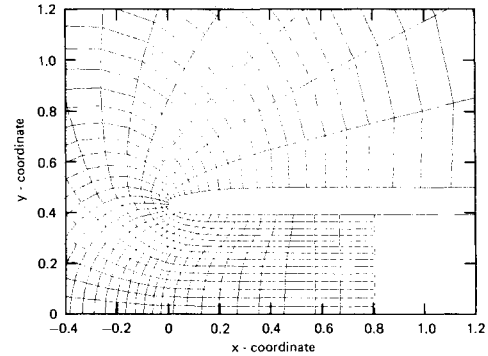

Fig. 3 Douglas research cowl contour and coordinate grid.

and

$$B=\begin{bmatrix} x_X^2 & y_X^2 & 2x_Xy_X & z_X^2 & 2x_Xz_X & 2y_Xz_X \\ x_Y^2 & y_Y^2 & 2x_Yy_Y & z_Y^2 & 2x_Yz_Y & 2y_Yz_Y \\ x_Xx_Y & y_Xy_Y & x_Xy_Y+x_Yy_X & z_Xz_Y & x_Xz_Y+x_Yz_X & y_Xz_Y+y_Yz_X \\ x_Z^2 & y_Z^2 & 2x_Zy_Z & z_Z^2 & 2x_Zz_Z & 2y_Zz_Z \\ x_Xx_Z & y_Xy_Z & x_Xy_Z+x_Zy_X & z_Xz_Z & x_Xz_Z+x_Zz_X & y_Xz_Z+y_Zz_X \\ x_Yx_Z & y_Xy_Z & x_Yy_Z+x_Zy_Y & z_Yz_Z & x_Yz_Z+x_Zz_Y & y_Yz_Z+y_Zz_Y \end{bmatrix}^{-1} \tag{10}$$

In Eqs. (8-10), matrices ***A***, ***B***, and ***C*** can be computed using Eqs. (1) and (2) and the three-dimensional relations. The elements of the matrices are then local functions of the physical coordinates of the mesh points.

Axisymmetric Nacelle at Angle of Attack

The ideas of the preceding section will now be applied to calculate the transonic flow about an axisymmetric inlet at an angle of attack. The complexity of the geometric approximations described previously can be simplified for this case. Consider x as the axial coordinate, y the radial coordinate ($y\equiv r$), z the azimuthal coordinate ($z\equiv\theta$), and X, Y, and Z the computational coordinates. If Z is identified with the azimuthal coordinate θ, then the same transformation of x,r to X, Y can be used for all Z when the geometry is axisymmetric. In this manner, the derivatives $x_Z, y_Z, z_X, z_Y, x_{XZ}, x_{ZZ}, x_{YZ}, y_{YZ}, z_{XY}, z_{XX}, z_{YY}, y_{ZZ}, x_{XZ}, z_{XZ}$, and z_{YZ} are all zero. This symmetry effectively uncouples the θ derivatives from those in the x-r plane with the result that Eqs. (6) and (7) can be written as

$$\begin{Bmatrix} \phi_x \\ \phi_r \end{Bmatrix} = \frac{1}{D}\begin{bmatrix} r_Y & -r_X \\ -x_Y & x_X \end{bmatrix}\begin{Bmatrix} \phi_X \\ \phi_Y \end{Bmatrix} \tag{11}$$

$$\phi_\theta = \phi_Z/\theta_Z \tag{12}$$

$$\begin{Bmatrix} \phi_{xx} \\ \phi_{rr} \\ \phi_{xr} \end{Bmatrix} = \frac{1}{D^2}\begin{bmatrix} r_Y^2 & r_X^2 & -2r_Yr_X \\ x_Y^2 & x_X^2 & -2x_Yx_X \\ -r_Yx_Y & -r_Xx_X & x_Xr_Y+x_Yr_X \end{bmatrix}\begin{Bmatrix} \phi_{XX}-x_{XX}\phi_x-r_{XX}\phi_r \\ \phi_{YY}-x_{YY}\phi_x-r_{YY}\phi_r \\ \phi_{XY}-x_{XY}\phi_x-r_{XY}\phi_r \end{Bmatrix} \tag{13}$$

$$\begin{Bmatrix} \phi_{\theta\theta} \\ \phi_{x\theta} \\ \phi_{r\theta} \end{Bmatrix} = \frac{1}{D\theta_Z}\begin{bmatrix} D/\theta_Z & 0 & 0 \\ 0 & r_Y & -r_X \\ 0 & -x_Y & x_X \end{bmatrix}\begin{Bmatrix} \phi_{ZZ}-\theta_{ZZ}\phi_\theta \\ \phi_{XZ} \\ \phi_{YZ} \end{Bmatrix} \tag{14}$$

where

$$D=x_Xr_Y-x_Yr_X \tag{15}$$

Along the axis of symmetry, cylindrical coordinates cannot be used, and a formulation in Cartesian coordinates will be considered. It is convenient to consider x along the axial direction, y perpendicular to the plane of symmetry, and z perpendicular to both x and y. Because of the symmetry and axisymmetry, values of $x_Y, x_Z, y_X, y_Z, z_X, z_Y, x_{XY}, x_{XZ}, x_{YZ}, y_{YY}, y_{YZ}, y_{XZ}, y_{ZZ}$ $y_{XX}, z_{XX}, z_{XY}, z_{YZ}, z_{ZZ}$, and z_{YY} are all zero, and

$$z_Z = y_Y \tag{16}$$

$$z_{XZ} = y_{XY} \tag{17}$$

$$x_{ZZ} = x_{YY} \tag{18}$$

The relation of the first derivatives of the potential function in the physical and computational planes is then given by Eqs. (11) and (12) with θ replaced by z. The second derivatives of the potential function in the physical plane, ϕ_{xx}, ϕ_{yy}, and ϕ_{xy} are related to the derivatives in the computational plane through Eq. (13) with r replaced by y, while the derivatives ϕ_{zz}, ϕ_{xz}, and ϕ_{yz} are given as

$$\begin{Bmatrix} \phi_{zz} \\ \phi_{xz} \\ \phi_{yz} \end{Bmatrix} = \frac{1}{Dz_Z}\begin{bmatrix} D/z_Z & 0 & 0 \\ 0 & y_Y & -y_X \\ 0 & -x_Y & x_X \end{bmatrix}\begin{Bmatrix} \phi_{ZZ}-x_{ZZ}\phi_x-z_{ZZ}\phi_z \\ \phi_{XZ}-z_{XZ}\phi_z \\ \phi_{YZ} \end{Bmatrix} \tag{19}$$

Through the application of Eqs. (11-14), and (19), the derivatives of the potential function in the physical plane can be computed for a given distribution of the potential function in the computational plane.

Grid Generation

For axisymmetric geometries, the grids generated in every r-x plane are the same. Therefore, the scheme applied in Ref. 4 to generate two-dimensional grids can be used to generate three-dimensional axisymmetric grids. A special mapping function and a sequence of shear transformations are used to transform the flowfield in each azimuthal plane into a rectangular domain, as shown in Fig. 2. The upper edge represents the cowl lip surface, the right edge represents the hub surface, the lower edge represents the axis of symmetry, and the left edge represents the far field boundary. Details of the mapping function have been presented in Ref. 4 and will not be duplicated here.

Governing Equation

The full potential equation to be solved is

$$(a^2-u^2)\phi_{xx}+(a^2-v^2)\phi_{rr}+(a^2-w^2)\frac{\phi_{\theta\theta}}{r^2}-2uv\phi_{xr}$$
$$-2uw\frac{\phi_{x\theta}}{r}-2vw\frac{\phi_{r\theta}}{r}+(a^2+w^2)\frac{\phi_r}{r}=0 \tag{20}$$

where u,v, and w are the x,r, and θ components of the flow velocity, respectively, and a is the local speed of sound, determined from the energy equation

$$a^2=a_0^2-\frac{\gamma-1}{2}\left(u^2+v^2+w^2\right) \tag{21}$$

where γ is the ratio of specific heats for the assumed calorically perfect gas and a_0 is the stagnation speed of sound. On the axis of symmetry, the equation is written in Cartesian coordinates oriented with $y=0$ representing the plane of symmetry; thus,

$$(a^2-u^2)\phi_{xx}+a^2\phi_{yy}+(a^2-w^2)\phi_{zz}-2uw\phi_{xz}=0 \tag{22}$$

where u and w represent the x and z components of the flow velocity, respectively.

Through the application of Eqs. (11-14), the full-potential equation written in the cylindrical coordinates, i.e., Eq. (20), can be rewritten in the computational coordinates, X, Y, and Z. Assume that the control point is located at point 13 where $X=Y=0$. The elements of the matrices in Eqs. (11-14) can be calculated as [consistent with Eqs. (1) and (2)]

$$x_X=\frac{1}{6}\left(2x_2+3x_{13}-6x_{16}+x_9\right) \tag{23a}$$

$$r_X=\frac{1}{6}\left(2r_2+3r_{13}-6r_{16}+r_9\right) \tag{23b}$$

$$x_Y=\frac{1}{6}\left(2x_{12}+3x_{13}-6x_{14}+x_5\right) \tag{23c}$$

$$x_{XX}=x_2-2x_{13}+x_{16} \tag{23d}$$

$$x_{XY}=\frac{1}{6}\left(2x_{X12}+3x_X-6x_{X14}+x_{X5}\right) \tag{23e}$$

...etc., where

$$x_{X12}=\frac{1}{6}\left(2x_1+3x_{12}-6x_{11}+x_{10}\right) \tag{24a}$$

$$x_{X14}=\frac{1}{6}\left(2x_3+3x_{14}-6x_{15}+x_8\right) \tag{24b}$$

$$x_{X5}=\frac{1}{6}\left(2x_4+3x_5-6x_6+x_7\right) \tag{24c}$$

The derivatives in the Z direction are calculated using conventional, centered, second-order-accurate formulas. It is convenient to recast the full-potential equation in coordinates aligned with the local flow direction s as

$$(a^2-q^2)\phi_{ss}+a^2(\nabla^2\phi-\phi_{ss})=0 \tag{25}$$

where

$$q^2=u^2+v^2+w^2 \tag{26}$$

$$\phi_{ss}=\frac{1}{q^2}\left(u^2\phi_{xx}+v^2\phi_{rr}+\frac{w^2}{r^2}\phi_{\theta\theta}+2uv\phi_{xr}\right.$$
$$\left.+2uw\frac{\phi_{x\theta}}{r}+2vw\frac{\phi_{r\theta}}{r}-w^2\frac{\phi_r}{r}\right) \tag{27}$$

and

$$\nabla^2=\phi_{xx}+\phi_{rr}+\frac{1}{r^2}\phi_{\theta\theta}+\frac{1}{r}\phi_r \tag{28}$$

Applying Eqs. (23) and substituting Eqs. (11-14) into Eqs. (27) and (28) yields

$$\phi_{ss}=\frac{1}{q^2}\left(p_1\phi_{XX}+p_2\phi_{YY}+p_3\phi_{XY}+p_4\phi_{ZZ}+p_5\phi_{XZ}\right.$$
$$\left.+p_6\phi_{YZ}+p_7\phi_X+p_8\phi_Y+p_9\phi_Z\right) \tag{29}$$

and

$$\nabla^2\phi=(h_1\phi_{XX}+h_2\phi_{YY}+h_3\phi_{XY}+h_4\phi_{ZZ}+h_5\phi_{XZ}$$
$$+h_6\phi_{YZ}+h_7\phi_X+h_8\phi_Y+h_9\phi_Z) \tag{30}$$

The coefficients $p_1,p_2,\ldots p_9,h_1,h_2,\ldots h_8$ and h_9 are functions of the physical coordinates of points 1,2,...,16 and the velocity components u,v, and w which are given as

$$u=\phi_x \tag{31}$$

$$v=\phi_r \tag{32}$$

$$w=\phi_\theta/r \tag{33}$$

where ϕ_x,ϕ_r, and ϕ_θ are related to ϕ_X,ϕ_Y, and ϕ_Z through Eqs. (11) and (12). Substituting Eqs. (29-33) into Eq. (25) yields the full-potential equation written in the computational coordinates.

Relaxation Solution

The full-potential equation thus obtained in the computational coordinates can be solved by relaxation. Jameson's rotated differencing scheme, similar to the one suggested in Refs. 3 and 4, will be adopted. The derivatives of the potential function in the full-potential equation can be approximated either by a third-order-accurate differencing scheme analogous to the geometric approximation (isoparametric representation) or by a second-order-accurate differencing scheme (superparametric representation) used in Ref. 4.

In the isoparametric representation, the same shape functions are used for both the geometric and potential function approximations in the X-Y plane, i.e.,

$$\phi=\psi^T\phi_i \tag{34}$$

where

$$\phi_i^T=[\phi_1,\phi_2,\ldots\phi_{15},\phi_{16}] \tag{35}$$

and $\phi_1, \phi_2, \ldots \phi_{15}$ and ϕ_{16} are values of ϕ at points 1,2,...15 and 16 (Fig.1). The derivatives of the potential function at the control point 13 are given as

$$\phi_X = \frac{1}{6}\left(2\phi_2 + 3\phi_{13} - 6\phi_{16} + \phi_9\right) \tag{36a}$$

$$\phi_Y = \frac{1}{6}\left(2\phi_{12} + 3\phi_{13} - 6\phi_{14} + \phi_5\right) \tag{36b}$$

$$\phi_{XX} = \phi_2 - 2\phi_{13} - \phi_{16} \tag{36c}$$

$$\phi_{YY} = \phi_{12} - 2\phi_{13} + \phi_{14} \tag{36d}$$

$$\phi_{XY} = \frac{1}{6}\left(2\phi_{X12} + 3\phi_X - 6\phi_{X14} + \phi_{X5}\right) \tag{36e}$$

where

$$\phi_{X12} = \frac{1}{6}\left(2\phi_1 + 3\phi_{12} - 6\phi_{11} + \phi_{10}\right) \tag{37a}$$

$$\phi_{X14} = \frac{1}{6}\left(2\phi_3 + 3\phi_{14} - 6\phi_{15} + \phi_8\right) \tag{37b}$$

$$\phi_{X5} = \frac{1}{6}\left(2\phi_4 + 3\phi_5 - 6\phi_6 + \phi_7\right) \tag{37c}$$

The accuracies of the first- and cross-derivatives thus obtained are third order, i.e., the truncation error is of the order of (ΔX^3) or (ΔY^3), while the discretization accuracies of the second derivatives are second order as in the conventional second-order differencing schemes. Therefore, with a given potential distribution, the velocity and pressure are more accurately defined, and the overall accuracy of the finite-difference approximation of the full-potential equation is improved mainly because of this higher-order representation of the velocity field and the higher-order coordinate transformation described previously. The potential gradients in the Z direction (i.e., azimuthal direction) are generally smaller than those in the X and Y directions; therefore, the derivatives in the Z direction are computed using the conventional second-order formula. One undesirable feature associated with the isoparametric approximation is that the first- and cross-derivatives of the potential functions in the X-Y plane are asymmetric. However, the convergence criterion of the relaxation equation is governed mainly by the second derivative terms. By properly considering the asymmetry of the first- and cross-derivative terms, a stable scheme can be constructed as follows.

In the computational domain, the direction of the velocity can be identified by the signs of the following vector,

$$\begin{Bmatrix} U \\ V \\ W \end{Bmatrix} = \begin{bmatrix} r_Y & -x_Y & 0 \\ -r_X & x_X & 0 \\ 0 & 0 & \dfrac{1}{r\,\theta_Z} \end{bmatrix} \begin{Bmatrix} u \\ v \\ w \end{Bmatrix} \tag{38}$$

A quasiconservative scheme can be constructed such that at supersonic points, an artificial viscosity term is added in conservation form such that the differencing of the ϕ_{ss} contribution in the first term of Eq. (25) is effectively upwind. For such a quasiconservative scheme, the artificial viscosity term H can be expressed as

$$H = (\mu f)_X + (\mu g)_Y + (\mu h)_Z \tag{39}$$

where

$$\mu = \max\left(1 - \frac{a^2}{q^2}, 0\right) \tag{40}$$

$$f = s_1(\Delta X)\left(p_1\phi_{XX} + p_3\phi_{XY} + p_5\phi_{XZ}\right) \tag{41}$$

$$g = s_2(\Delta Y)\left(p_2\phi_{YY} + p_3\phi_{XY} + p_6\phi_{YZ}\right) \tag{42}$$

$$h = s_3(\Delta Z)\left(p_4\phi_{ZZ} + p_5\phi_{XZ} + p_6\phi_{YZ}\right) \tag{43}$$

$$s_1 = 1 \text{ if } U > 0; \quad -1 \text{ if } U < 0 \tag{44}$$

$$s_2 = 1 \text{ if } V > 0; \quad -1 \text{ if } V < 0 \tag{45}$$

$$s_3 = 1 \text{ if } W > 0; \quad -1 \text{ if } W < 0 \tag{46}$$

The finite-difference equations resulting from the above formulation are highly implicit. To ensure that the relaxation scheme corresponds to a convergent process, the old and updated values of the potential function ϕ and ϕ^+ must be mixed properly.[3,6] A stable scheme to solve Eq. (25) can be constructed using Eq. (36) and results in the following equation for the correction $c_{i,j,k} = \phi^+_{i,j,k} - \phi_{i,j,k}$ to be added to the potential at each point,

$$\begin{aligned} &\alpha_1\left(c_{i,j,k} - c_{i,j+s_2,k}\right) + \alpha_2\left(c_{i,j,k} - c_{i,j,k+s_2,k}\right) \\ &+ \alpha_3\left(c_{i,j,k} - c_{i,j-2s_{2,k}}\right) + \alpha_4\left(c_{i,j,k} - c_{i,j,k-s_3}\right) \\ &+ \alpha_5\left(c_{i,j,k} - c_{i-s_1,j,k}\right) + \alpha_6\left(c_{i,j,k} - c_{i-2s_1,j,k}\right) \\ &+ \alpha_7 c_{i,j,k} + c_{XY} = R \end{aligned} \tag{47}$$

where R is the residual of Eqs. (20) or (22) evaluated with values of the potential from previous iteration, and

$$\begin{aligned} \alpha_1 = {} & a^2h_2 - p_2 - s_2\left(a^2h_8 - p_8\right) + 1.5\,\mu p_2 + \omega_s\left(s_1U \right. \\ & \left. + s_2V + s_3W\right)V(s_2 - 1)/2D + s_1s_2\left(a^2h_3 - p_3\right) \end{aligned} \tag{48}$$

$$\begin{aligned} \alpha_2 = {} & a^2h_2 - p_2 + s_2\left(a^2h_8 - p_8\right) + 6\,\mu p_2 \\ & + \omega_2\left(s_1U + s_2V + s_3W\right)V(s_2 + 1)/2D - s_1s_2 \\ & \times \left(a^2h_3 - p_3\right)/2 \end{aligned} \tag{49}$$

$$\alpha_3 = -s_2\left(a^2h_8 - p_8\right)/6 - 3\,\mu p_2 + s_1s_2\left(a^2h_3 - p_3\right)/12 \tag{50}$$

$$\alpha_4 = a^2h_4 - p_4 + 6\,\mu p_4 + \omega_s\left(s_1U + s_2V + s_3W\right)W/D \tag{51}$$

$$\begin{aligned} \alpha_5 = {} & a^2h_1 - p_1 + s_1\left(a^2h_7 - p_7\right) + 6\,\mu p_1 + \omega_s\left(s_1U + s_2V \right. \\ & \left. + s_3W\right)U/D - s_1s_2\left(a^2h_3 - p_3\right)/2 \end{aligned} \tag{52}$$

$$\alpha_6 = s_1s_2\left(a^2h_3 - p_2\right)/12 - s_2\left(a^2h_7 - p_7\right)/6 - 3\,\mu p_1 \tag{53}$$

$$\begin{aligned} \alpha_7 = {} & \left[\left(2/\omega_r\right) - 1\right]\left(a^2h_1 - p_1 + a^2h_4 - p_4\right) \\ & \times \max\left(0, a^2 - q^2\right)/\left(a^2 - q^2\right) + \alpha_{XY} \end{aligned} \tag{54}$$

where ω_r is a subsonic over-relaxation factor lying between 1 and 2, and ω_s governs the amount of the ϕ_{sl} term[3,4] added to stabilize the iteration. The term c_{XY} in Eq. (47) and the last terms in Eqs. (48-50), and (52) and α_{XY} are consistent with the use of the updated values of ϕ in lines $i - s_1$, $i - 2_1$, and $i - 3s_1$ in evaluating ϕ_{XY}. Equation (47) is implicit in the Y direction; i.e., its solution must be obtained by Y line relaxation. A discussion of results obtained by this higher-order relaxation equation will be provided later.

In the so-called superparametric representation, the order of the potential function approximation is lower than the

order of the geometric approximation.[7] This representation is useful for cases when the degree of distortion of the coordinate lines is greater than the rate of change of the potential function. Consider a hybrid element, where the geometric approximation is made in a third-order element described previously, and the potential function approximation is made in a second-order element described in Ref. 4,

$$\phi \neq \overset{*}{\psi}{}^{T} \phi_k \tag{55}$$

where

$$\phi_k^T = [\phi_1, \phi_2, \phi_3, \phi_{14}, \phi_{15}, \phi_{16}, \phi_{11}, \phi_{12}, \phi_{13}] \tag{56}$$

and $\overset{*}{\psi}$ is the corresponding column vector of second-order element shape functions which has been described in Ref. 4. The three-dimensional, finite-difference formula to be shown are obtained as extensions of the two-dimensional formulation presented in Ref. 4. Applying Eqs. (25), (29), (30), (39), and (55), a relaxation equation can be obtained as shown in Eq. (47) with

$$\alpha_3 = \alpha_6 = c_{XY} = 0 \tag{57}$$

$$\alpha_1 = a^2 h_2 - p_2 + \mu p_2 + \omega_s (s_1 U + s_2 V + s_3 W) V (s_2 - 1)/2D \tag{58}$$

$$\alpha_2 = a^2 h_2 - p_2 + \mu (3p_2 + p_3 + p_6) + \omega_s (s_1 U + s_2 V + s_3 W) V (s_2 + 1)/2D \tag{59}$$

$$\alpha_4 = a^2 h_4 - p_4 + \mu (3p_4 + p_5 + p_6) \tag{60}$$

$$\alpha_5 = a^2 h_1 - p_1 + \mu (3p_1 + p_3 + p_5) + \omega_s (s_1 U + s_2 V + s_3 W) U/D \tag{61}$$

and

$$\alpha_7 = [(2/\omega_r) - 1] (a^2 h_1 - p_1 + a^2 h_4 - p_4) \times \max(0, a^2 - q^2)/(a^2 - q^2) \tag{62}$$

The major difference of these coefficients from those obtained by Caughey and Jameson[3] comes from the expression of ϕ_{ss} and $\nabla^2 \phi$. The ϕ_{ss} and $\nabla^2 \phi$ expressions given in Ref. 3 include only their principal parts.

Boundary Conditions

In order to eliminate the singularity in the velocity potential at infinity outside the nacelle, the potential function ϕ is expressed as

$$\phi = U_\infty x \cos\alpha + U_\infty r \sin\theta \sin\alpha + G \tag{63}$$

where U_∞ is the freestream velocity, α the angle of attack, θ is zero in the horizontal plane perpendicular to the plane of symmetry and equal to $\pi/2$ and $-\pi/2$ on the windward and lee sides, respectively, and G is determined numerically. The boundary condition at infinity outside the nacelle is then $G \equiv 0$.

The surface boundary conditions for axisymmetric nacelles are independent of the velocity component in the θ direction. Along the lip surface, $Y = \text{const}$, the boundary condition is

$$v/u = y_X/x_X \tag{64}$$

and along the hub surface, $X = \text{const}$, the boundary condition is

$$v/u = y_Y/x_Y \tag{65}$$

These two boundary conditions are applied to determine the value of the potential function at surface points. Along the lip surface, the velocity components, u and v can be evaluated using Eqs. (31), (32), and (11). In the third-order element, the lip surface always lies along the edge 1-12-11-10, and the value of the potential function at point 12 is to be determined. Applying Eqs. (1), (2), and (34) at point 12 yields

$$x_X = (2x_1 + 3x_{12} - 6x_{11} + x_{10})/6 \tag{66a}$$

$$y_X = (2y_1 + 3y_{12} - 6y_{11} + y_{10})/6 \tag{66b}$$

$$x_Y = (11x_{12} - 18x_{13} + 9x_{14} - 2x_5)/6 \tag{66c}$$

$$y_Y = (11y_{12} - 18y_{13} + 9y_{14} - 2y_5)/6 \tag{66d}$$

$$\phi_X = (2\phi_1 + 3\phi_{12} - 6\phi_{11} + \phi_{10})/6 \tag{66e}$$

$$\phi_Y = (11\phi_{12} - 18\phi_{13} + 9\phi_{14} - 2\phi_5)/6 \tag{66f}$$

If the values of $\phi_{13}, \phi_{14}, \phi_5, \phi_1, \phi_{11}$, and ϕ_{10} are known, the value of ϕ_{12} can be determined by applying Eqs. (11), (31), (32), (64), and (66). Similarly, the boundary condition along the hub surface, Eq. (65), can be applied to determine the values of the potential function at the hub surface.

The boundary condition at downstream infinity inside the nacelle is specified to be a prescribed, uniform axial velocity that can be obtained by using the isentropic mass flux relation for a given mass flow ratio or for a given one-dimensional Mach number at the lip throat.

Computational Considerations

The line-relaxation scheme described in the previous sections solves the potential functions along $X = \text{constant}$ and $Z = \text{constant}$ lines. It sweeps along the X direction first, and then along the Z direction. When sweeping in the X direction, it starts at the highlight of the cowl lip and sweeps toward the downstream infinities inside and outside the nacelle alternatively, as in Ref. 4. When sweeping in the Z direction, it starts at the windward side and sweeps toward the lee side. The $\theta = \text{constant}$ planes are so arranged that there is always a $\theta = 0$ deg plane perpendicular to the plane of symmetry, and the values of the potential function along the axis of symmetry are solved only in the $\theta = 0$ deg plane. In other words, except in the $\theta = 0$ deg plane, the values of the potential function along the Y lines are solved from the point next to the axis of symmetry to the point next to the lip surface. When solving the potential function in the windward-side plane of symmetry, a stable scheme is established by approximating the correction at $k - s_3$ by the correction at $k + s_3$ in the previous iteration. The sweep direction and the schematic mesh cell in the computational X-Y plane are shown in Fig. 2. The dots in the cells are the control points where the potential functions are solved by requiring that the difference approximation of the potential equation be satisfied, based on the information within the cells.

It is well known that the convergence rate of the relaxation scheme suffers as the mesh spacing approaches zero, because the spectral radius of the relaxation matrix approaches unity for most elliptic problems. This difficulty can be partially overcome by using a sequence of meshes. In all the calculations presented here, a sequence of two or three meshes is used depending on the accuracy requirement of each individual problem. The converged solution obtained in the previous mesh is used as the initial solution for the next finer mesh. Furthermore, the ultimate improvement of the convergence rate is obtained by incorporating an extrapolated acceleration scheme as in Refs. 8 and 9. Details of the schemes can be found in Refs. 8 and 9. Although the scheme was applied to solve two-dimensional problems in those

references, the extension to treating three-dimensional problems is straightforward.

Numerical Results

An accuracy study of the two-dimensional solutions obtained by using the second order, third order, and hybrid elements is presented in Figs. 3-6. In Fig. 4, the pressure distributions obtained by the present schemes for an axisymmetric nacelle engine inlet without centerbody shown in Fig. 3 are compared with experiment[10] and with results obtained by a second-order-accurate scheme.[4] A coordinate grid of the inlet is also shown in Fig. 3. The freestream Mach number M_∞ is 0.7, the mass flow ratio 0.7, and the angle of attack zero. The intermediate-mesh (48×14) solution obtained by using the third-order element agrees better with the fine-mesh (96×28) solution than the solutions obtained using the second order and the hybrid elements. The second-order-element solution predicts slightly lower C_P's near the peaks and a slightly higher C_p distribution on the outer surface. The hybrid-element solution predicts the C_p distribution well on the outer surface, but predicts a higher C_p distribution on the inner surface. The maximum residuals at the end of the computation for the results shown in the figure are 10^{-6}. The residual is normalized by the square of the stagnation speed of sound divided by the local element area. The number of relaxation steps required to reach this maximum residual in the intermediate mesh is about 160 using the third-order element, 210 using the second-order element, and 110 using the hybrid element. The improved convergence rate obtained with the third-order and hybrid elements may be due to rapid elimination of the local mesh errors during early relaxation steps. Computations performed using the hybrid element show better convergence rates than those performed with the third-order element; all the derivatives of the potential function expressed in the hybrid element are symmetric, while only the second derivative of the potential function in the third-order element is symmetric. The fine-mesh solutions obtained using these three types of elements agree to within the accuracy of the plotted figure. The two-dimensional program occupies 120 k (octal) storage on the Cyber 175, and the CPU time per sweep in a 48×14 mesh is about 0.122 s using the third-order element, 0.114 s using the hybrid element, and 0.097 s using the second-order element. Although the third-order element requires about 25% more CPU time per sweep than the second-order element, the improvement in overall accuracy of the solutions for a given mesh results in a net gain in computational efficiency. In Fig. 6, the Mach number distributions obtained in the intermediate mesh (48×16) using the three types of elements are compared with the fine mesh (96×32) solution and the experiment[11] for a 13.97 cm diam inlet shown in Fig. 5. Figure 5 also shows the coordinate grid of the intermediate mesh. The freestream Mach number is 0.127, the one-dimensional Mach number at the cowl lip throat is 0.496, and the angle of attack is zero. The fine-mesh solutions obtained using the three types of elements agree within the accuracy of the plotted figures. During the iterative process, the maximum correction is reduced by three or four orders of magnitude. By this time, the Mach number distribution is essentially converged. There is no significant improvement of the convergence rate observed in the relaxation process with the third-order and the

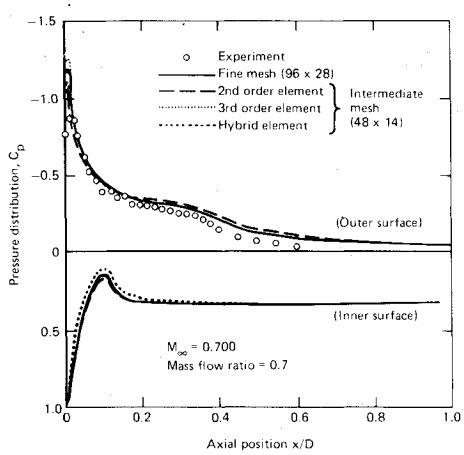

Fig. 4 Accuracy study, pressure distribution on the surface of Douglas research cowl.

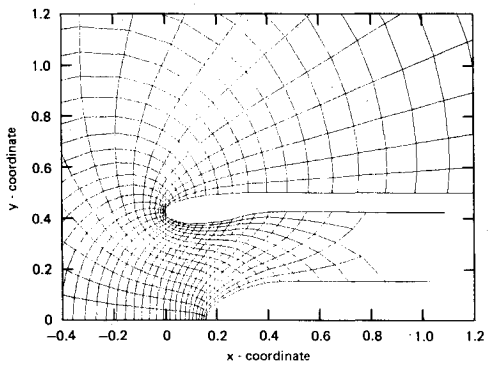

Fig. 5 A 13.97 cm diam inlet contour and coordinate grid.

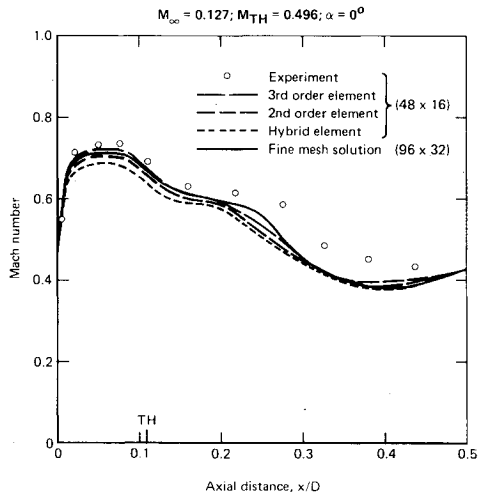

Fig. 6 Accuracy study, Mach number distribution on the inner surface of a centerbody inlet.

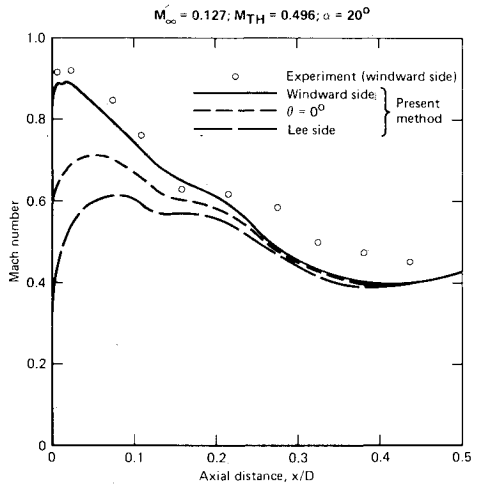

Fig. 7 Mach number distribution on the inner surface of a centerbody inlet for $\alpha = 20$ deg.

hybrid elements. None of the intermediate-mesh solutions converge to the fine-mesh solution. However, the intermediate-mesh solution obtained using the third-order element agrees with the fine-mesh solution everywhere except near an inflection point on the lip inner contour near $x/D=0.25$. The agreement between the fine-mesh solution and the experiment is generally good, except after $x/D=0.25$ where separation was observed in the experiment. The hybrid-element solution obtained in Fig. 6 is obviously no better than the second-order element solution. No satisfactory explanation has been found yet. The fine-mesh solutions obtained in Figs. 4 and 6 are considered to be the converged solutions, since the differences between the intermediate- and fine-mesh solutions are negligible when the third-order element is used.

The effects of angle of attack are presented in Figs. 7-9. In Figs. 7 and 8, the same engine inlet as in Fig. 5 is considered, the freestream Mach number is 0.127, the Mach number at the cowl lip throat M_{TH} is 0.496, and the angle of attack is 20 deg and 40 deg, respectively, for the results shown in Figs. 7 and 8. A sequence of two meshes is used. In the coarse mesh, there are 31 mesh points along X, 11 mesh points along Y, and 3 mesh points along Z. In the fine mesh, the number of mesh points along the three directions is doubled. Four-hundred relaxation steps are used in both the coarse and the fine meshes, and the maximum correction at the end of calculation generally is reduced by four orders of magnitude in the coarse mesh and three orders of magnitude in the fine mesh. The hybrid element is used in all three-dimensional calculations. The three-dimensional program occupies 300 k (octal) storage on the Cyber 175, and the CPU time per sweep in the fine mesh is about 1.39 s, and the total CPU time required for a typical run is about 11 min on a Cyber 175. In Figs. 7 and 8, the Mach number distributions along the inner surface of the cowl lip on the windward side, lee side, and $\theta=0$ deg planes are plotted vs the axial distance normalized by the maximum outer diameter. The calculated Mach number distributions on the windward side are slightly below the experimental data, but the difference is small except downstream of $x/D=0.25$ where separation occurs. In Figs. 9a, 9b, and 9c, the effect of angle of attack is studied for the engine inlet shown in Fig. 3

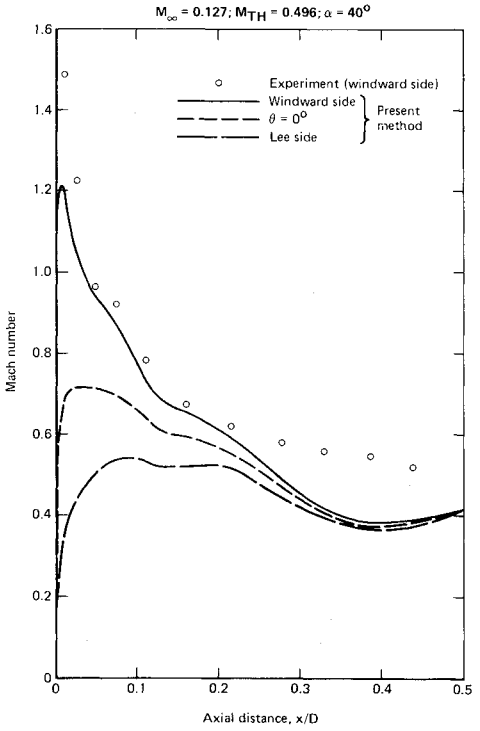

Fig. 8 Mach number distribution on the inner surface of a centerbody inlet for $\alpha=40$ deg.

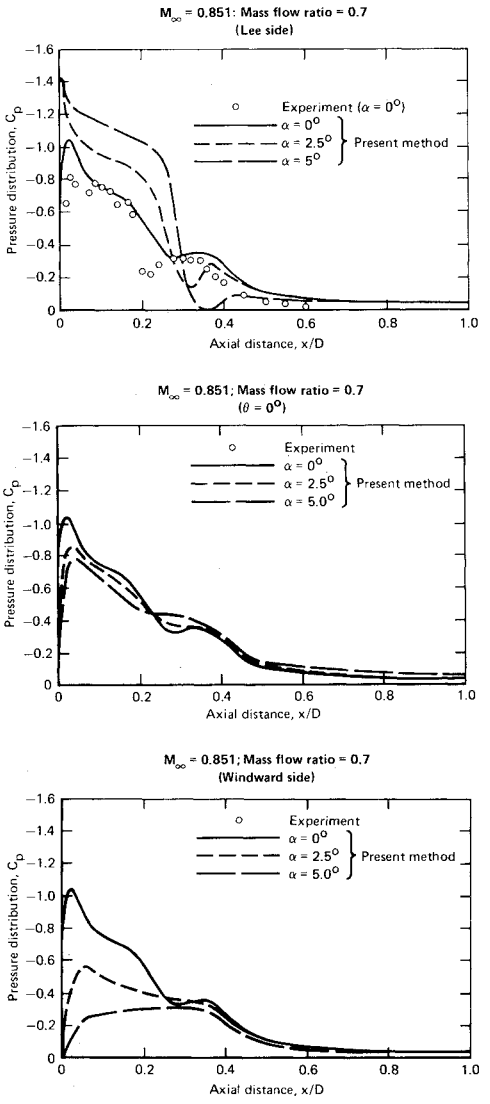

Fig. 9 Effect of angle of attack, preasure distribution on the outer cowl lip surface; a) lee side, b) $\theta=0$ deg plane, c) windward side.

for high subsonic freestream Mach number cases. The freestream Mach number is 0.851, and the mass flow ratio is 0.7. The pressure distributions on the outer surface of the cowl lip are shown for 0, 2.5, and 5 deg angles of attack. The results obtained on a $60\times16\times5$ mesh on the lee side, $\theta=0$ deg, and windward-side planes are presented in Figs. 9a, 9b, and 9c, respectively. The numerical results for zero angle of attack are compared with experiment[10] in Fig. 9a. The numerically predicted shock location for the zero angle-of-attack case is behind the measured position in the experiment. This is due mainly to the general characteristics of the quasi-conservation scheme. Because of the relatively sparse mesh near the shock, the pressure distribution is less sharply defined. The experimental data for nonzero angle of attack were unavailable for this study. On the lee side, the numerical results show that increasing the angle of attack causes an increase of the shock strength and a slightly downstreamward movement of the shock location. This trend is reversed on the windward side.

Concluding Remarks

A higher-order, finite-difference scheme using a third-order shape function has been introduced and applied to solve transonic potential flowfields around axisymmetric nacelles with or without centerbodies. The effect of the angle of attack is also studied. Two types of elements are proposed. In the third-order element, both the geometry and the potential

function are approximated using third-order shape functions. In the hybrid element, the geometry is approximated using third-order shape functions and the potential function is approximated using second-order shape functions. The solutions obtained using the third-order element generally provide better accuracy within a given mesh than those obtained using the second-order and the hybrid elements. In some cases, solutions obtained using the hybrid element have better convergence rates than those from the other two elements.

The application of the scheme is not limited to axisymmetric geometries. Since the grid generation scheme is uncoupled from the flow equation solver, the grids for fully three-dimensional geometries can be generated cross section by cross section analytically or numerically and the extension of the present scheme to arbitrary, complex three-dimensional geometry involves little additional complexity in treating the body boundary conditions. However, the computing cost may be increased by a factor of 3-5 because a 6×6 matrix equation must be solved, instead of two 3×3 matrix equations.

Acknowledgment

This work was supported by the McDonnell Douglas Corporation Independent Research and Development Program.

References

[1] Murman, E.M. and Cole, J.D., "Calculation of Plane Steady Transonic Flows," *AIAA Journal,* Vol. 9, Jan. 1971, pp. 114-121.

[2] Jameson, A. and Caughey, D.A., "A Finite Volume Method for Transonic Potential Flow Calculations," *Proceedings of AIAA 3rd Computational Fluid Dynamics Conference,* Albuquerque, N. Mex. June 1977, pp. 35-54.

[3] Caughey, D.A. and Jameson, A., "Numerical Calculation of Transonic Potential Flow About Wing-Body Combinations," *AIAA Journal,* Vol. 17, Feb. 1979, pp. 175-181.

[4] Chen, L.T. and Caughey, D.A., "Calculation of Transonic Inlet Flowfields Using Generalized Coordinates," *Journal of Aircraft,* Vol. 17, March 1980, pp. 167-174.

[5] Reyhner, T.A., "Transonic Potential Flow Around Axisymmetric Inlets and Bodies at Angle-of-Attack," *AIAA Journal,* Vol. 15, Sept. 1977, pp. 1299-1306.

[6] Jameson, A., "Iterative Solution of Transonic Flows Over Airfoils and Wings, Including Flows at Mach 1," *Communications on Pure and Applied Mathematics,* Vol. 27, 1974, pp. 283-309.

[7] Gallagher, R.H., *Finite Element Analysis: Fundamentals,* Prentice-Hall, Englewood Cliffs, N.J., 1974.

[8] Caughey, D.A. and Jameson, A., "Accelerated Iterative Calculation of Transonic Nacelle Flowfields," *AIAA Journal,* Vol. 15, Oct. 1977, pp. 1474-1480.

[9] Chen, L.T. and Caughey, D.A., "Transonic Inlet Flow Calculations Using a General Grid Generation Scheme," Symposium on Primary, Non-Rotating Passages in Turbomachines, ASME Winter Annual Meeting, New York, N.Y., Dec. 1979, pp. 125-132.

[10] Unpublished data, Douglas Aircraft Company, Long Beach, Calif.

[11] Felderman, E.J. and Albers, A., "Comparison of Experimental and Theoretical Boundary-Layer Separation for Inlets at Incidence Angle at Low-Speed Conditions," NASA TM X-3194, Feb. 1975.